Chemical Science

ROYAL SOCIETY OF CHEMISTRY

EDGE ARTICLE

View Article Online
View Journal | View Issue

Cite this: *Chem. Sci.*, 2025, **16**, 18152

All publication charges for this article have been paid for by the Royal Society of Chemistry

Received 10th July 2025
Accepted 28th August 2025

DOI: 10.1039/d5sc05135e

rsc.li/chemical-science

Dual-function synergy in boron-doped Fe–N–C: enhanced site density and intrinsic activity

Jinjing Tao,†[ab] Xin Guan,†[ab] Xiaolong Yang,[ab] Jingsen Bai,[ab] Chuanfu Li,[ab] Xiaohui Liu,[ab] Minhua Shao,[def] Meiling Xiao,*[abc] Changpeng Liu*[abc] and Wei Xing*[abc]

Atomically dispersed transition metal, nitrogen co-doped carbon (M–N–C) is hailed as the most promising platinum alternative for the oxygen reduction reaction (ORR); however, its practical deployment is bottlenecked by inferior intrinsic activity and insufficient site density. Herein, we report a sodium borohydride ($NaBH_4$) assisted synthesis strategy to achieve dual enhancement of active site density and intrinsic activity. This strategy endows a B-doped catalyst (denoted as Fe–sZ8–N–C) with a high active site density of 2.26×10^{20} sites per g, a two-fold enhancement over conventional Fe–N–C. Besides, the intrinsic activity of the catalyst is improved from 0.96 e per site per s to 1.5 e per site per s. Density functional theory (DFT) calculations reveal that the boron-modulated coordination structure switches the ORR pathway from associative OOH dissociation to direct O_2 cleavage while weakening intermediate adsorption strength, thereby boosting intrinsic activity. When assembled in practical PEMFC devices, the optimized Fe–sZ8–N–C catalyst delivers an exceptional peak power density of 1.3 W cm^{-2} under H_2–O_2 conditions at 80 °C, demonstrating its potential for fuel cell applications.

1 Introduction

Fuel cells enable the direct conversion of chemical energy into electric energy, offering inherent advantages in hydrogen utilization efficiency.[1,2] Currently, proton exchange membrane fuel cells (PEMFCs) represent a leading technology due to their high power density and operational reliability.[3] However, their widespread deployment is hindered by the sluggish kinetics of the oxygen reduction reaction (ORR) at the cathode, which hinders the development of PEMFCs. Although noble metal platinum (Pt)-based electrocatalysts exhibit excellent catalytic performance for the ORR, the high cost and scarcity of Pt restrict their large-scale implementation.[4,5] In this regard, the development of non-noble metal catalysts has emerged as a critical research direction in the fuel cell community. Fortunately, atomically dispersed transition metal, nitrogen co-doped carbon (M–N–C) has been developed as a highly promising alternative to Pt-based electrocatalysts.[6,7]

Current strategies to enhance their ORR activity focus on: (i) optimizing the intrinsic activity of active sites,[8–10] (ii) increasing the density of active sites,[8,11–13] and (iii) improving active site utilization.[14–16] Considerable progress has been achieved in research focusing on the aforementioned strategies over the past few decades. For example, Shui *et al.* used SiO_2 as a template to enrich micropores in a carbon substrate, thereby increasing active site density.[13] For intrinsic activity optimization, heteroatom doping (such as P, S, N, *etc.*) or secondary metal incorporation has been employed, primarily by modulating the electronic structure of active sites.[17–20] Such a regulation in the electronic states is beneficial for addressing the suboptimal adsorption energetics of reaction intermediates on conventional M–N–C catalysts, which represent an inherent limitation dictated by the Sabatier principle. Nevertheless, these initiatives focus exclusively on a single aspect of performance enhancement. Dai and his colleagues, for instance, increased the density of active sites through increasing metal loadings but observed negligible improvement in the intrinsic activity. Such isolated enhancement ultimately constrains the overall catalytic performance, thereby resulting in considerable performance disparity between the state-of-the-art M–N–C catalysts and Pt/C

[a]*State Key Laboratory of Electroanalytic Chemistry, Jilin Province Key Laboratory of Low Carbon Chemistry Power, Jilin Provincial Science and Technology Innovation Center of Hydrogen Energy, Changchun Institute of Applied Chemistry, Chinese Academy of Sciences, Changchun, 130022, China. E-mail: mlxiao@ciac.ac.cn; liuchp@ciac.ac.cn; xingwei@ciac.ac.cn*

[b]*School of Applied Chemistry and Engineering, University of Science and Technology of China, Hefei, 230026, China*

[c]*CIAC – HKUST Joint Laboratory for Hydrogen Energy, Changchun, 130022, China*

[d]*Department of Chemical and Biological Engineering, The Hong Kong University of Science and Technology, Clear Water Bay, Kowloon, Hong Kong 999077, China*

[e]*CIAC-HKUST Joint Laboratory for Hydrogen Energy, Energy Institute, The Hong Kong University of Science and Technology, Clear Watery Bay, Kowloon 999077, Hong Kong, China*

[f]*Guangzhou Key Laboratory of Electrochemical Energy Storage Technologies, Fok Ying Tung Research Institute, The Hong Kong University of Science and Technology, Guangzhou 511458, China*

† These authors contributed equally to this work.

benchmarks.[21] Thus, the rational integration of intrinsic activity optimization and active site densification represents a viable pathway toward high-performance M–N–C catalysts.

Herein, we rationally designed a boron-doped Fe–N–C catalyst with enriched active site density *via* a $NaBH_4$ mediated high-temperature pyrolysis approach. Advanced structural characterization, including X-ray adsorption near-edge structure (XANES) and extended X-ray absorption fine structure (EXAFS) analyses, confirms the successful incorporation of B into the first-shell coordination of Fe–N–C and the tailored electronic states caused by B doping, which is in line with density functional theory (DFT) calculations. This regulation in turn optimizes the adsorption strength of oxygen-containing intermediates and switches the reaction pathway from the conventional *OOH dissociation to the direct $*O_2$ cleavage route, thereby enhancing intrinsic activity. Besides, the addition of $NaBH_4$ elevates the solution pH, facilitating the precipitation of Fe ions and ultimately enriching the metal content in the synthesized precursor; as a result, the B-doped catalyst (Fe–sZ8–N–C) exhibits higher active site density compared to its undoped counterpart (labelled as Fe–Z8–N–C). This synergistic enhancement of both intrinsic activity and site density results in superior electrochemical performance in acidic electrolyte, showing a 43 mV positive shift in half-wave potential ($E_{1/2}$). More impressively, the excellent catalytic performance is further demonstrated in the PEMFC test with a peak power density of 1.3 W cm^{-2}, manifesting the huge potential of the as-developed Fe–sZ8–N–C cathode for fuel cell applications.

2 Results and discussion

2.1 Morphology and structure characterization

The typical synthesis process of Fe–sZ8–N–C is depicted in Fig. 1a. Sodium borohydride ($NaBH_4$) was selected as a boron source, and zeolitic imidazolate framework-8 (ZIF-8) served as a catalyst support precursor due to its high nitrogen content. Upon reacting with methanol, the pH of the solution increases and the negatively charged boron-containing species enhance the adsorption of Fe^{3+}, thereby increasing the density of active sites. Beyond that, the introduction of $NaBH_4$ dramatically accelerates the synthesis rate and yield of ZIF-8, offering advantages in time and cost efficiency for catalyst production. To determine whether the crystal structure of ZIF-8 was altered upon $NaBH_4$ introduction, we employed X-ray diffraction (XRD) analysis (Fig. S1). The diffraction peaks of Fe–sZ8 (without heat treatment) coincide with those of Fe–Z8, confirming that the crystal structure remains unchanged even with excess $NaBH_4$. Scanning electron microscopy (SEM) images reveal a topographical change from a regular dodecahedral morphology of Fe–Z8 to a small-sized nanosphere of Fe–sZ8 (45 nm) (Fig. S2 and S3). As particle size reduction of the support material has been linked to enhanced catalytic activity,[22] we anticipated that the Fe–sZ8 derived catalyst (Fe–sZ8–N–C) would exhibit improved performance.

After high-temperature calcination, there is no significant change in the morphological structure of Fe–Z8–N–C and Fe–sZ8–N–C catalysts, as shown in the SEM images (Fig. S4). A closer observation of the transmission electron microscopy (TEM) images reveals that no visible metal particles were found for Fe–sZ8–N–C (Fig. 1c), whereas some aggregates can be discerned in Fe–Z8–N–C (Fig. 1b).[23,24] The absence of metallic iron species in Fe–sZ8–N–C is further confirmed by the predominant broad peaks at 26° and 44° of XRD patterns, corresponding to the (002) and (101) planes of amorphous carbon, respectively (Fig. S5).[25] In contrast, Fe–Z8–N–C shows sharp peaks at 43° and 50°, characteristic of Fe_5C_2 crystalline phases.[26] These results indicate that introduction of $NaBH_4$ promotes iron atom anchoring, favouring single-atom site formation. To verify B doping in the Fe–sZ8–N–C catalyst, energy dispersive spectroscopy (EDS) elemental mapping was performed (Fig. 1d and S6). Distinct boron signals are observed, confirming successful doping. Concurrently, enhanced iron signals in Fe–sZ8–N–C *versus* Fe–Z8–N–C suggest higher iron content in the former, coinciding with enhanced iron content detected in Fe–sZ8–N–C (3.67 wt% *vs.* 2.67 wt% for Fe–Z8–N–C) using the inductively coupled plasma (ICP) method (Table S1). These findings demonstrate that $NaBH_4$-mediated synthesis enables increased active site density. To directly discern the active site, we then resorted to aberration-corrected high-angle-annular dark field scanning transmission electron microscopy (AC-HAADF-STEM), showing high-density atomic sites (Fig. 1e). In addition to this, we observed the formation of atomic pair-like structures with an interatomic distance of ~0.32 nm (Fig. 1f). Such close Fe–Fe proximity likely originates from the exceptionally high site density in the catalyst, forcing partial atomic overlap.

The B dopant effect on the microstructure of the pyrolyzed carbon substrates, *i.e.*, surface area and graphitic degree that are important parameters for M–N–C electrocatalysts, was carefully examined by the N_2 adsorption–desorption technique and Raman spectroscopy, respectively. Brunauer–Emmett–Teller (BET) analysis reveals comparable specific surface areas for Fe–sZ8–N–C (884.5 $m^2\ g^{-1}$) and Fe–Z8–N–C (899.4 $m^2\ g^{-1}$) catalysts (Fig. 1g), while Fe–sZ8–N–C exhibits a substantially larger total pore volume (1.285 $cm^3\ g^{-1}$) than Fe–Z8–N–C (0.109 $cm^3\ g^{-1}$), indicating enhanced pore abundance of Fe–sZ8–N–C that facilitates efficient mass transport (Fig. S7).[27] Raman spectral analysis (Fig. S8 and S9) reveals key structural characteristics of the carbon materials. Peak deconvolution yields four distinct components, and the ratios of peak intensities serve as important indicators, such as the defect degree (I_D/I_G) and doping extent (I_{D3}/I_G).[22] While both catalysts exhibit a similar defect degree (I_D/I_G is 1.32), Fe–sZ8–N–C demonstrates marginally higher heteroatom doping than Fe–Z8–N–C (0.56 *vs.* 0.54 of I_{D3}/I_G), attributable to the doping of boron species.

To probe the surface composition and electronic structures of catalysts, X-ray photoelectron spectroscopy (XPS) was conducted (Fig. 2a). The high-resolution N 1s XPS spectra are deconvoluted into five peaks including pyridinic N (398.4 eV), Fe–N_x (399.0 eV), pyrrolic N (400.0 eV), graphitic N (401.2 eV) and oxidized N (402.9 eV).[28,29] Notably, Fe–sZ8–N–C exhibits significantly higher Fe–N_x content than Fe–Z8–N–C, confirming enhanced active site density. Moreover, the Fe–N_x peak displays a distinct negative binding energy shift, implying a boron dopant-induced electronic modulation effect. The relatively

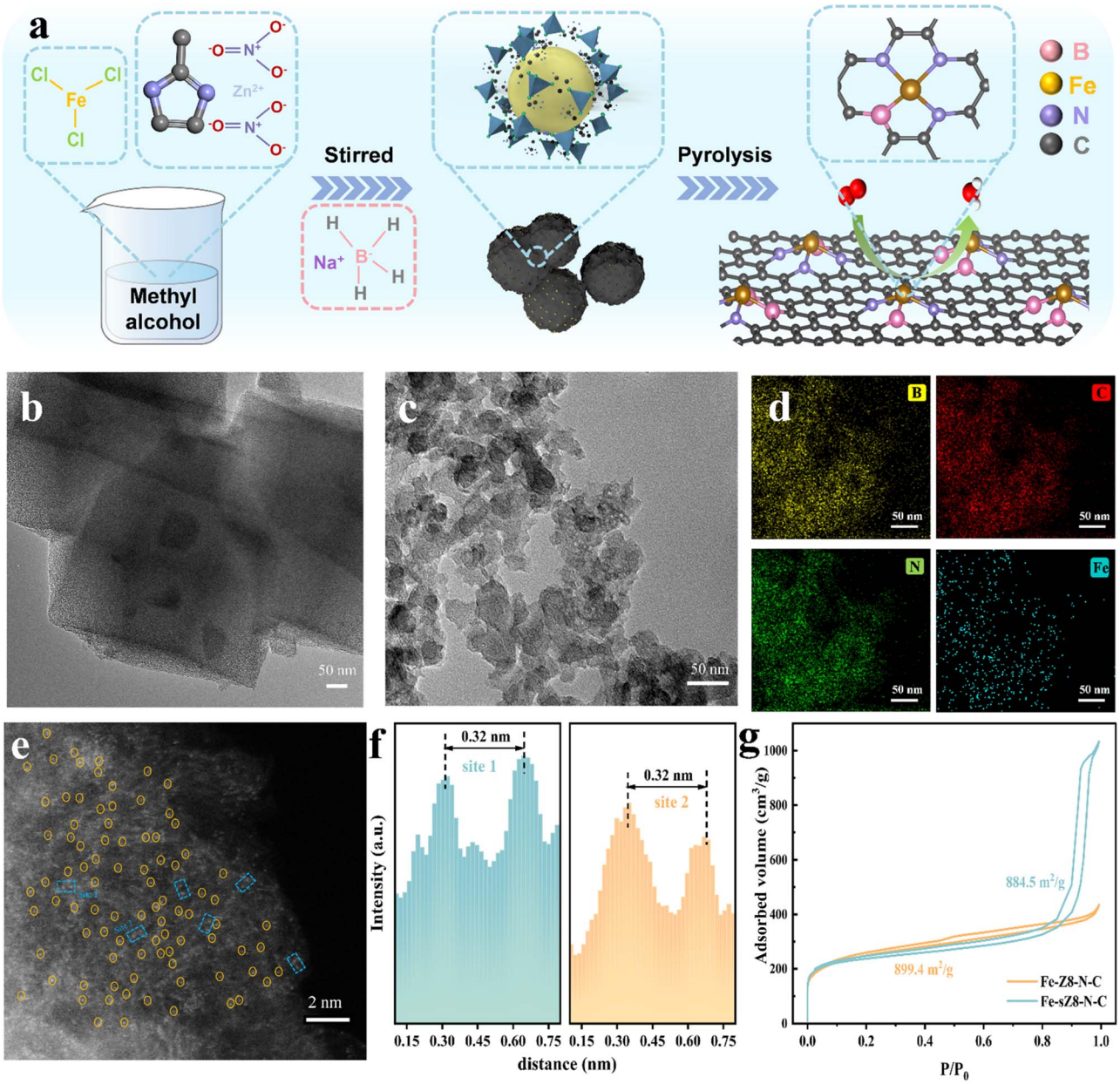

Fig. 1 (a) Schematic illustration of the preparation of the Fe–sZ8–N–C catalyst. (b) TEM image of Fe–Z8–N–C and (c) Fe–sZ8–N–C. (d) EDS mapping of Fe–sZ8–N–C. (red: C, green: N, yellow: B, and blue: Fe). (e) HAADF-STEM image of Fe–sZ8–N–C, the Fe single atoms and paired Fe atoms are marked by yellow circles and blue rectangles, respectively. (f) The corresponding intensity profile of sites 1 and 2 in (e). (g) N_2 adsorption–desorption isotherm of Fe–Z8–N–C and Fe–sZ8–N–C.

weak electron-withdrawing capacity of B compared to N results in increased electron density around the Fe center, thereby elongating the Fe–N bond, which can be confirmed by the data in Table S2. The electronic redistribution results in attenuating the Fe–N bonding interaction and reducing its binding strength.

Besides, quantitative XPS analysis indicates a boron content of 0.36 at% (Table S1), and the B 1s XPS spectrum of Fe–sZ8–N–C (Fig. S10) confirms the successful incorporation of B into Fe–sZ8–N–C. High-resolution Fe 2p XPS analysis reveals Fe^{2+} predominance in Fe–sZ8–N–C, whereas Fe^{3+} dominates in Fe–Z8–N–C (Fig. S11). This observation further demonstrates that B doping alters the electronic configuration of the catalytic sites.[30]

To precisely examine the B doping effect on the active site structure, we synthesized a control B-free single-atom catalyst (denoted as Fe–Z8–N–C-L) with reduced Fe loading, eliminating interference from Fe nanoparticles. X-ray absorption spectroscopy (XAS) was conducted to investigate the coordination environment and electronic state changes. Fe K-edge X-ray absorption near-edge structure (XANES) spectra (Fig. 2b) reveal that the absorption edges of Fe–Z8–N–C-L and Fe–sZ8–N–C are between those of Fe foil and Fe_3O_4, indicating that the

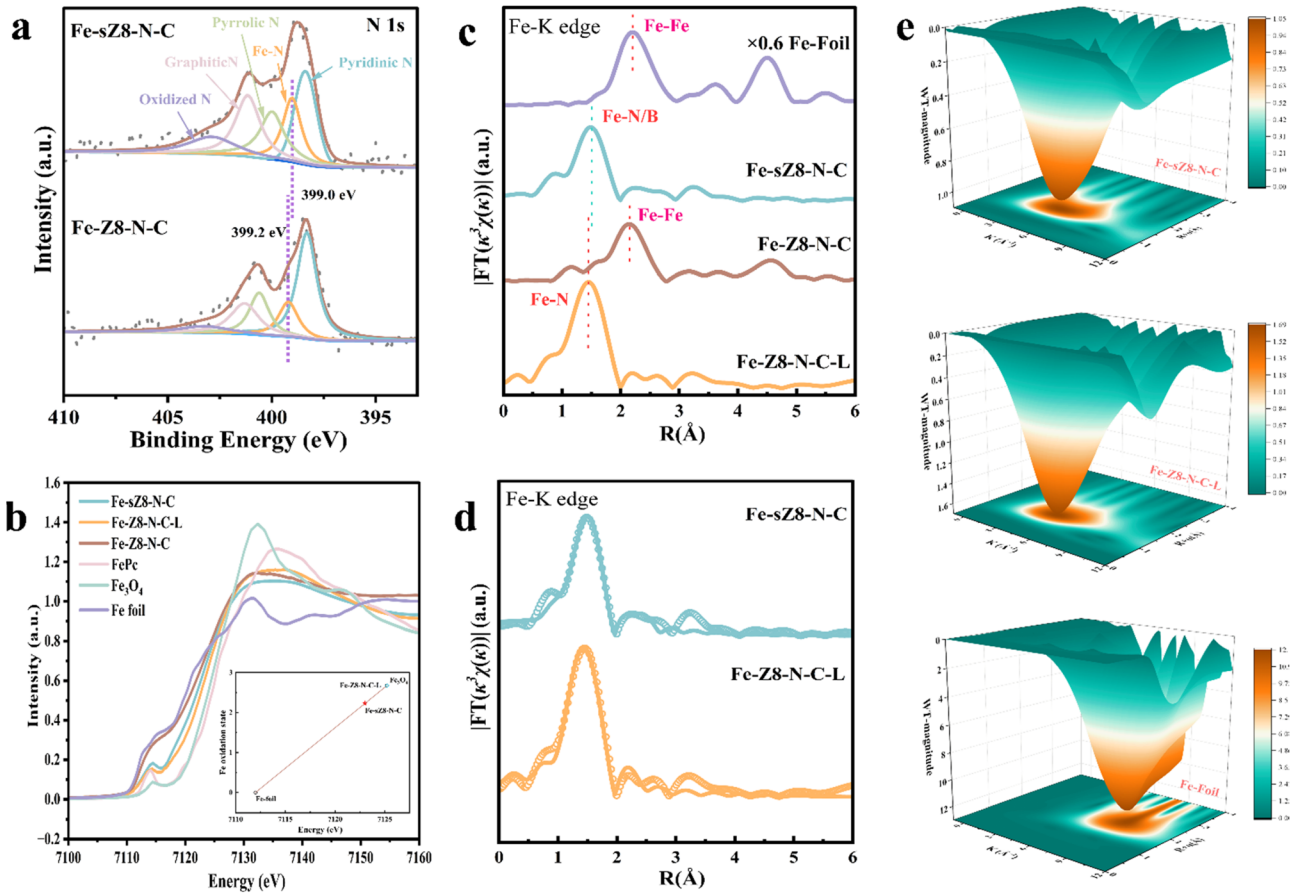

Fig. 2 (a) High-resolution N 1s XPS spectra and (b) Fe K-edge XANES spectra of Fe–sZ8–N–C and other references. (c) k^3-Weighted Fourier-transformed EXAFS spectra for Fe–sZ8–N–C, Fe–Z8–N–C and the other references. (d) Experimental and best fitting Fe K-edge EXAFS curves for Fe–sZ8–N–C and Fe–Z8–N–C-L in *R*-space. (e) k^3-Weighted wavelet transformed Fe K-edge EXAFS spectra of Fe–sZ8–N–C, Fe–Z8–N–C-L and Fe foil.

valence states of Fe for both samples are between 0 and +3. It should be noted that the absorption edge energy of Fe–sZ8–N–C is lower than that of Fe–Z8–N–C-L, corresponding to a decreased valence state of Fe in Fe–sZ8–N–C. In contrast, Fe–Z8–N–C exhibits an absorption edge close to the Fe foil, which demonstrates the presence of metallic nanoparticles in Fe–Z8–N–C, consistent with the TEM observations.[31] Fourier-transformed extended X-ray absorption fine structure (FT-EXAFS) spectra can provide the atomic-scale structure information of catalysts, as shown in Fig. 2c. Both Fe–SZ8–N–C and Fe–Z8–N–C-L exhibit a dominant peak at ~1.5 Å (phase-uncorrected), while no discernible Fe–Fe scattering (~2.2 Å) is observed, confirming the dominance of single-atom Fe sites without metallic nanoparticles,[32] which is further corroborated by complementary TEM and XRD analyses of Fe–Z8–N–C-L (Fig. S12 and S13). Crucially, Fe–sZ8–N–C shows a slight positive shift in the peak position compared to Fe–Z8–N–C-L, likely attributable to the weaker electron-withdrawing capability of B. This reduces electron transfer from Fe to N/B ligands, weakening bonding interactions and elongating bond distances. These observations are perfectly consistent with our XANES and N 1s XPS interpretations. To determine the precise coordination number and bond length, FT-EXAFS fitting was performed (Fig. 2d). Fe–SZ8–N–C adopts a hybrid configuration with 1.5 Fe–N and 2.5 Fe–B coordination (Table S2), elegantly demonstrating the coexistence of Fe–N_2B_2 and Fe–N_3B motifs. In striking contrast, Fe–Z8–N–C shows a conventional Fe–N_4 configuration. The wavelet-transform EXAFS spectra (Fig. 2e) provide crystalline clarity: both materials exhibit maximal intensity at ~4.9 $Å^{-1}$ in *k*-space, while remaining entirely devoid of the higher *k* (~8 $Å^{-1}$) signatures characteristic of Fe–Fe metallic bonding.

2.2 ORR performance

Linear sweep voltammetry (LSV) was employed to evaluate the ORR activities of the as-prepared catalysts in an O_2-saturated 0.1 M $HClO_4$ electrolyte, and all potentials are relative to the reversible hydrogen electrode (RHE). As shown in Fig. 3a, Fe–sZ8–N–C exhibits superior ORR catalytic activity compared to Fe–Z8–N–C, as evidenced by more positive onset potential (E_{onset}: 0.975 V *vs.* 0.902 V for Fe–Z8–N–C) and half-wave potential ($E_{1/2}$: 0.835 V *vs.* 0.792 V for Fe–Z8–N–C). In addition, we systematically optimized the catalyst performance by adjusting the amount of $NaBH_4$ used in the synthesis. As shown

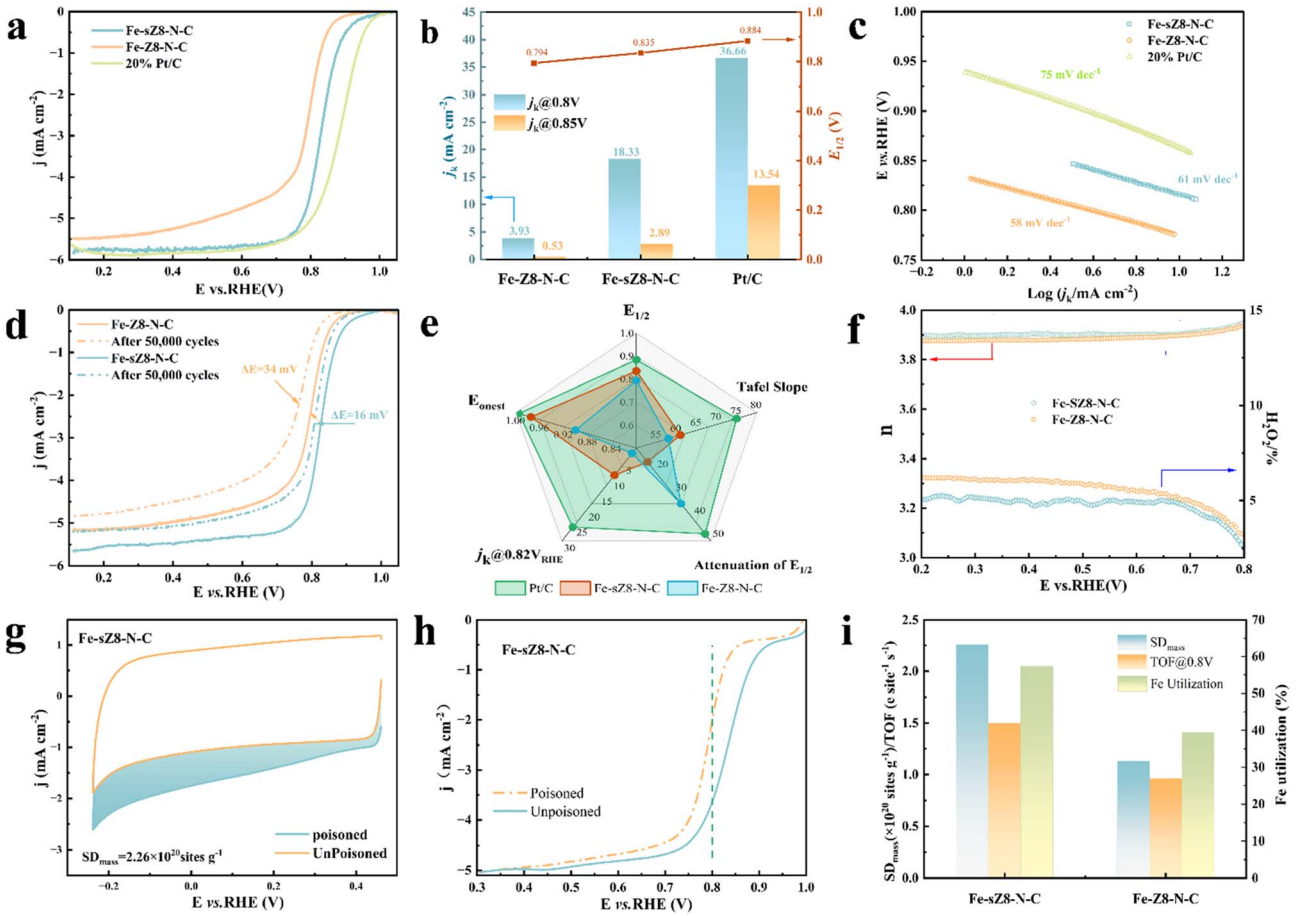

Fig. 3 (a) ORR polarization curves, (b) $E_{1/2}$ and j_k at 0.8 V and 0.85 V, and (c) Tafel slope curves of Fe–sZ8–N–C, Fe–Z8–N–C and commercial Pt/C catalysts in 0.1 M $HClO_4$. (d) ORR polarization curves of Fe–sZ8–N–C and Fe–Z8–N–C before and after 50 000 CV cycles. (e) Comparison of $E_{1/2}$, E_{onset}, and j_k at 0.82 V, Tafel slope and attenuation of $E_{1/2}$ for Fe–sZ8–N–C, Fe–Z8–N–C and commercial Pt/C catalysts in 0.1 M $HClO_4$. (f) H_2O_2 yield and electron transfer number (n) of Fe–sZ8–N–C and Fe–Z8–N–C. (g) Nitrite stripping voltammetry for Fe–sZ8–N–C in N_2-saturated 0.5 M acetate electrolyte buffer (pH = 5.2). (h) O_2 reduction polarization curves of Fe–sZ8–N–C at unpoisoned and poisoned stages of the *in situ* nitrite stripping protocol. (i) Comparison of SD_{mass}, TOF and Fe utilization efficiency among Fe–sZ8–N–C and Fe–Z8–N–C.

in Fig. S14, the introduction of $NaBH_4$ significantly enhanced the catalytic activity in all cases and the optimal half-wave potential was achieved using 0.2 g of $NaBH_4$. The performance improvement validates the feasibility of our strategy for boosting the activity of M–N–C catalysts. Remarkably, even upon drastic reduction of Fe loading to achieve single-atom dispersion, the catalytic activity of Fe–Z8–N–C-L remained largely preserved, unambiguously demonstrating the predominant role of isolated single-atom active sites in governing the catalytic process (Fig. S15). Analysis of kinetic current densities (j_k) at 0.85 V shows that Fe–sZ8–N–C achieves 5× higher j_k than Fe–Z8–N–C (Fig. 3b), with similar enhancements observed at 0.8 V.

The ORR mechanism was then studied by Tafel analysis, showing nearly identical slopes for Fe–sZ8–N–C (61 mV dec^{-1}) and Fe–Z8–N–C (58 mV dec^{-1}). This indicates a shared rate-determining step during the ORR (Fig. 3c and S16). To further assess the long-term operational stability, all catalysts were subjected to accelerated stress testing (AST) consisting of 50 000 cyclic voltammetry (CV) scans between 0.95 and 0.6 V *versus* RHE in O_2-saturated 0.1 M $HClO_4$ electrolyte. As evidenced by the polarization curves in Fig. 3d and S17, the Fe–sZ8–N–C catalyst demonstrates exceptional electrochemical stability, exhibiting merely a 16 mV negative shift in $E_{1/2}$ after AST, significantly lower than the 34 mV degradation observed for Fe–Z8–N–C and 47 mV for benchmark Pt/C. More remarkably, detailed kinetic analysis reveals that Fe–sZ8–N–C maintains superior activity to Fe–Z8–N–C, as evidenced by its higher kinetic current density (j_k) at 0.82 V (Fig. 3e). Motivated by these findings, we conducted rotating ring-disk electrode (RRDE) measurements to quantitatively evaluate the $2e^-/4e^-$ ORR pathway selectivity by monitoring H_2O_2 production. As illustrated in Fig. 3f, Fe–sZ8–N–C achieves a H_2O_2 yield of <5% and an electron transfer number (n) of >3.9, outperforming Fe–Z8–N–C and Fe–Z8–N–C-L (Fig. S18). In line with the RRDE results, Koutecky–Levich (K–L) equation analysis further validates a near-ideal four electron transfer pathway (Fig. S19). This exceptional $4e^-$ selectivity of Fe–sZ8–N–C minimizes Fenton-type degradation by suppressing $^{\bullet}OH$ radical generation from

peroxide intermediates, rationalizing its outstanding durability during AST.[33,34]

While B incorporation demonstrably boosts catalytic activity, the observed metal loading variations necessitate a more nuanced assessment of the underlying enhancement mechanism. The active site density (SD_{mass}) and turnover frequency (TOF) provide critical insights. A nitrite poisoning experiment was carried out to quantify SD_{mass} and thus the intrinsic TOF values.[11,35] As depicted in Fig. 3g and S20, the site density of Fe–sZ8–N–C is 2.26×10^{20} sites per g, which is twice that of Fe–Z8–N–C (1.13×10^{20} sites per g). Pre- and post-poisoning LSV analysis reveals TOF values of 1.5 e per site per s for Fe–sZ8–N–C *versus* 0.96 e per site per s for Fe–Z8–N–C (Fig. 3h and S20). These results demonstrate simultaneous enhancement in both active site density and intrinsic activity on Fe–sZ8–N–C. Fe atom utilization rates were estimated to be 57.3% and 39.4% for Fe–sZ8–N–C and Fe–Z8–N–C, respectively (Fig. 3i). In summary, the sodium borohydride-synthesized catalyst exhibits superior performance, primarily attributed to: (1) markedly enhanced active-site density enabled by $NaBH_4$ and (2) boron-triggered coordination transformation from Fe–N_4 to Fe–N_2B_2 configuration that optimizes the electronic structure and intrinsic activity of catalytic sites.

To evaluate the practical viability of our catalysts for proton exchange membrane fuel cells (PEMFCs), Fe–sZ8–N–C and Fe–Z8–N–C were employed as cathode catalysts and commercial Pt/C as the anode catalyst in the membrane electrode assemblies (MEAs) for PEMFC performance testing. Notably, after B doping, the open-circuit voltage of Fe–sZ8–N–C increased by nearly 60 mV under practice environments (H_2–O_2-2 bar) and the maximum power density of Fe–sZ8–N–C is 1.3 W cm^{-2}, which is approximately 1.9-fold higher than that of Fe–Z8–N–C (0.675 W cm^{-2}) (Fig. 4a). The results of the tests under H_2–air-2 bar conditions also showed the same trend, where Fe–sZ8–N–C exhibits a higher open-circuit voltage (0.910 V *vs.* 0.856 V) and a 1.9× greater peak power density (0.55 *vs.* 0.295 W cm^{-2}) (Fig. 4b). The evaluation of the intrinsic activity of catalysts in membrane electrodes can also be compared based on the current density under the same test conditions. As shown in Fig. S21, under H_2–air conditions at 0.8 V, while the achieved current density of 70 mA cm^{-2} for Fe–sZ8–N–C still falls short of the 2025 DOE target, its substantial 75% improvement over Fe–sZ8–N–C (40 mA cm^{-2}) highlights remarkable progress in catalytic performance. This further demonstrates that the intrinsic activity of Fe–sZ8–N–C is superior to that of Fe–Z8–N–C. To evaluate the catalyst stability under fuel cell operating conditions, AST was performed. As shown in Fig. 4c, after 30 000 cycles, the Fe–sZ8–N–C catalyst exhibited a decrease in peak power density from 700 to 600 mW cm^{-2}, corresponding to a decay of approximately 15%. In contrast, the Fe–Z8–N–C catalyst showed a more pronounced degradation of 22%. These results demonstrate the superior stability of Fe–sZ8–N–C. Consequently, combining the active site density of the catalyst with the peak power density of the catalyst under H_2–air-1 bar conditions, the fuel cell performance of Fe–sZ8–N–C is superior to that of most reported catalysts (Fig. 4d).[8,11,13,21,29,30,36–39]

The polarization curves of PEMFC tests reveal that performance degradation of Fe–Z8–N–C primarily stems from ohmic polarization in the mid-potential region, which is mainly caused by proton and electron transport resistances. To

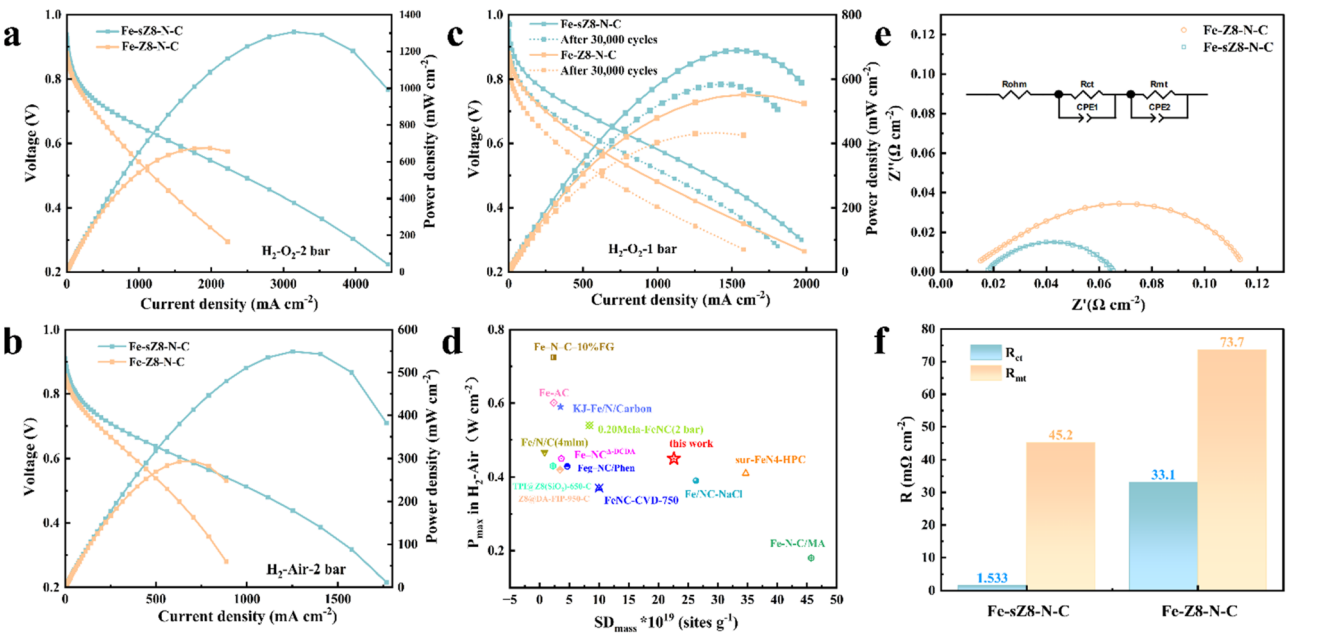

Fig. 4 Polarization and power density curves of (a) H_2–O_2-2 bar and (b) H_2–air-2 bar PEMFCs using Fe–sZ8–N–C and Fe–Z8–N–C as cathode catalysts. (c) Polarization and power density curves of Fe–sZ8–N–C and Fe–Z8–N–C under H_2–O_2-1 bar conditions before and after 30 000 cycles of AST. (d) PEMFC performance comparison among Fe–sZ8–N–C and the previously reported Fe–N–C catalysts. (e) Nyquist plots for PEMFCs with the indicated cathode catalysts at a potential of 0.6 V and the inset shows the equivalent circuit model, and (f) R_{ct} and R_{mt} of Fe–sZ8–N–C and Fe–Z8–N–C obtained by EIS fitting (test conditions: 80 °C and 100% relative humidity).

elucidate the superior performance of Fe–sZ8–N–C under operational conditions, we conducted electrochemical impedance spectroscopy (EIS) analysis at 0.6 V to probe its charge transfer characteristics (Fig. 4e). The Nyquist plots were fitted using an equivalent Randles circuit model (inset of Fig. 4e). The fitting results (Fig. 4f) demonstrate that Fe–sZ8–N–C exhibits significantly lower charge transfer resistance (R_{ct} = 1.533 mΩ cm^{-2}) compared to Fe–Z8–N–C (R_{ct} = 33.1 mΩ cm^{-2}), indicating more efficient oxygen reduction kinetics. This improvement is further supported by the reduced mass transport resistance (R_{mt}) observed for Fe–sZ8–N–C (45.2 mΩ cm^{-2} *vs.* 73.7 mΩ cm^{-2} for Fe–Z8–N–C), which we attribute to its hierarchical mesoporous architecture (as shown in Fig. 1g). The significantly lower R_{ct} and R_{mt} of Fe–sZ8–N–C, as evidenced by EIS, directly correlate with its improved fuel cell performance.

2.3 Mechanistic study

We further elucidated the mechanistic role of boron doping in enhancing Fe–N–C catalytic activity through first-principles density functional theory (DFT). The Fe–N(B)–C configurations were constructed based on experimental characterization data, where FeN_2B_2 and FeN_3B sites coexist with an exothermic formation energy of −7.39 eV, confirming thermodynamic stability (Fig. 5a). Charge density difference plots (Fig. 5b) reveal distinct charge redistribution in the asymmetric FeN_2B_2 and FeN_3B sites compared to the pristine symmetric FeN_4 structure (Fig. 5c), demonstrating B doping-induced electronic symmetry breaking. Bader charge analysis quantifies charge transfer from Fe to the surrounding environment. The number of electrons transferred is 0.74*e*, 0.79*e* and 1.09*e* for FeN_2B_2, FeN_3B and FeN_4, respectively, indicating a lower valence state of Fe in B-doped systems, in line with XANES analyses. We modelled ORR pathways on FeN_2B_2 and FeN_3B, beginning with FeN_2B_2. Initial O_2 adsorption studies reveal three configurations, *i.e.*, side-on bridging Fe–B (O_2-side on@B), side-on Fe (O_2-side on@Fe), and end-on Fe with adsorption energies of −0.34 eV, −0.29 eV and 0.14 eV, respectively, suggesting more favourable side-on adsorption (Fig. S22). Crystal orbital Hamilton population (COHP) analysis further confirms stronger orbital interactions between the O atom and the substrate for O_2-side on@B, evidenced by a more negative integrated COHP value compared with O_2-side on@Fe (Fig. 5d–f). This enhanced Fe–B synergistic binding facilitates O–O bond scission, prompting a dissociative pathway: O_2 → *O + *OH → *OH + *OH → $2H_2O$. The conventional associative pathway (O_2 → *OOH → *O → *OH → H_2O) is precluded by the inability to form stable *OOH. Free energy calculations (Fig. 5g) identify *OH desorption (*OH + OH → $2H_2O$) as the rate-determining step (RDS) with an overpotential (η) of 0.57 V (Fig. 5g). To experimentally probe the ORR pathway on Fe–sZ8–N–C, we conducted *in situ* infrared spectroscopy (IR) to monitor intermediate species formation

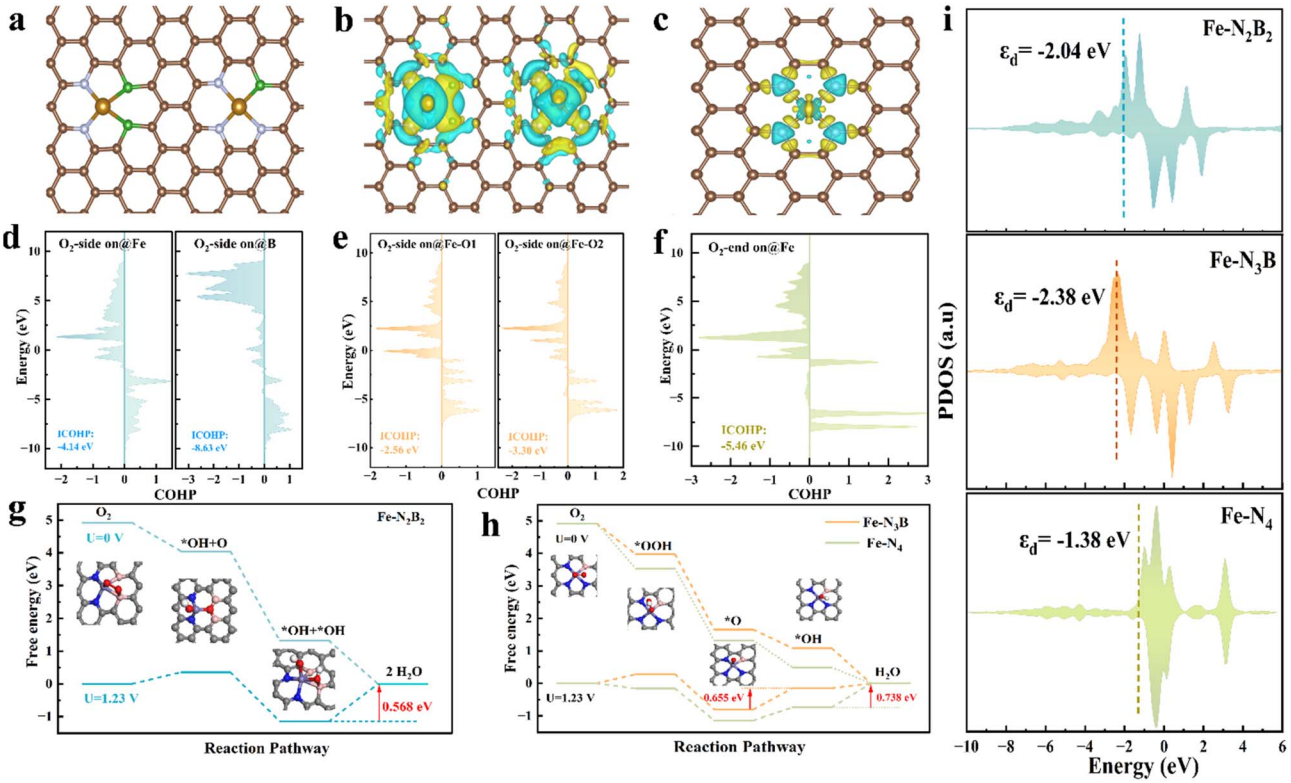

Fig. 5 DFT calculations. (a) Illustration of the atomic arrangement showing the coexistence of FeN_2B_2 and FeN_3B sites. Charge density difference plots of (b) FeN_2B_2 (left) and FeN_3B (right) sites; (c) FeN_4 site. COHP of FeN_2B_2 for (d) O_2 adsorbed on Fe–B in a side-on mode; (e) O_2 adsorbed on Fe in a side-on mode; (f) O_2 adsorbed on Fe in an end-on mode. ORR free energy diagrams of (g) the FeN_2B_2 site (Fe and B as active centres); (h) FeN_3B and FeN_4 sites. (i) PDOS of the Fe d-band in FeN_2B_2, FeN_3B and FeN_4 sites.

under reaction conditions. As illustrated in Fig. S23, the Fe–Z8–N–C exhibits a well-defined peak at approximately 1215 cm^{-1}, assigned to the intermediate species *OOH. In contrast, Fe–sZ8–N–C shows no detectable signal in this region, indicating the absence of accumulated *OOH during the ORR. This absence suggests that O_2 undergoes direct cleavage on Fe–sZ8–N–C rather than proceeding through conventional associative pathways. This experimental observation is consistent with our DFT calculations, which predicted a modified reaction mechanism due to boron incorporation. We propose that boron doping within the first-shell coordination of Fe–N–C active site facilitates direct O–O bond scission, thereby altering the reaction pathway and significantly enhancing the overall ORR activity.

Subsequent investigation of the ORR mechanism on FeN_3B commenced with competitive O_2 adsorption configuration screening, revealing side-on O_2–Fe–B-2 ($E_{ad} = -1.79$ eV) as energetically unfavourable compared to side-on O_2–Fe-2 ($E_{ad} = -3.00$ eV) and end-on adsorption ($E_{ad} = -3.03$ eV) (Fig. S24). Thus, O_2 tends to adsorb on FeN_3B in the end-on configuration. Notably, oxygen adsorption exclusively occurs at the Fe active site rather than N atoms, proceeding through *OOH formation. This intermediate undergoes protonation to *O or dissociates to *O + *OH, with the reaction energies of −2.31 and −1.91 eV, respectively. Thus, the ORR follows the conventional associative pathway ($O_2 \rightarrow$ *OOH $\rightarrow$ *O $\rightarrow$ *OH $\rightarrow H_2O$) on FeN_3B, consistent with FeN_4. As shown in Fig. 5h, the ORR Gibbs free energy diagrams for FeN_3B and FeN_4 at $U = 0$ V and $U = 1.23$ V reveal that the RDS is *O hydrogenation to *OH for FeN_3B sites with an overpotential η of 0.655 V, whereas it turns out to be *OH desorption for FeN_4 sites ($\eta = 0.738$ V).[40,41]

Besides, projected density of states (PDOS) analysis that can probe the electron rearrangement of the orbital level was performed to gain insights into the electronic modulation induced by B doping. As shown in Fig. 5i, the Fe 3d states of the FeN_2B_2 and FeN_3B configurations exhibit significant energy shifts away from the Fermi energy level, compared to FeN_4. Consistently, the calculated d-band centre of both FeN_2B_2 (−2.04 eV) and FeN_3B (−2.38 eV) resides at a more negative energy than that of FeN_4 (−1.38 eV), which implies weakened adsorption strength of oxygen-containing intermediates on FeN_2B_2 and FeN_3B. The optimized adsorbate–catalyst interaction would improve catalytic activity by facilitating intermediate desorption. These results strongly demonstrate that the B-doping strategy can tailor the adsorption mode of O_2, thus modifying the reaction path of the ORR and adjusting the rate-determining step of the ORR. Besides, boron incorporation reduces the adsorption intensity of oxygen intermediate species at the catalyst active site, resulting in enhanced intrinsic activity.[32]

3 Conclusions

In summary, we have successfully synthesized B-doped Fe–N–C catalysts using sodium borohydride. Fe–sZ8–N–C developed in this work demonstrates exceptional electrochemical performance, particularly in PEMFC applications, achieving a peak power density of 1.3 W cm^{-2} and activity (70 mA cm^{-2} at 0.8 V), a 1.9-fold improvement over conventional Fe–Z8–N–C. To systematically elucidate the origin of this enhanced performance, we employed a combined experimental and computational approach (DFT calculations) and identified three key contributing factors: first, boron doping induces a transformation of active sites from planar Fe–N_4 to distorted Fe–N_2B_2 or Fe–N_3B configurations, which not only alters the ORR pathway but also significantly reduces the overpotential of the rate-determining step. Furthermore, the catalyst exhibits an exceptionally high density of active sites (2.26×10^{20} sites per g *vs.* 1.13×10^{20} sites per g for Fe–Z8–N–C), while simultaneously maintaining a hierarchical mesoporous architecture that facilitates efficient mass transport within the membrane electrode assembly. In light of this, these synergistic effects explain the superior activity of Fe–sZ8–N–C, positioning it as a promising, cost-effective alternative to Pt-based catalysts for practical PEMFC applications.

Author contributions

Jinjing Tao and Xin Guan: methodology, investigation, formal analysis and writing – original draft. Xiaolong Yang and Jingsen Bai: methodology and investigation. Chuanfu Li and Xiaohui Liu: investigation and validation. Minhua Shao: conceptualization and supervision. Meiling Xiao, Changpeng Liu and Wei Xing: funding acquisition, conceptualization, supervision and writing – review and editing.

Conflicts of interest

There are no conflicts to declare.

Data availability

The data supporting this article have been included as part of the SI.

Supplementary information: General information, detailed experimental procedures, characterization data for catalysts, and computational details. See DOI: **https://doi.org/10.1039/d5sc05135e**.

Acknowledgements

The authors thank the National Key Research and Development Program of China (2022YFB4004100), the National Natural Science Foundation of China (22272161, 22179126), and the Jilin Province Science and Technology Development Program (20240101019JC) for financial support. The authors thank the Shanghai Synchrotron Radiation Facility for conducting the X-ray absorption spectroscopy experiments at the BL20U station. The experiment was carried out using a Rotating Ring-Disk Electrode (DC-DSR ROTATOR, PHYCHEMI) and Fuel Cell Testing System (DC-980pro, PHYCHEMI) from Phychemi Co.

References

1 J. Zhang, H. Yang and B. Liu, *Adv. Energy Mater.*, 2020, **11**, e2002473.
2 S. M. Alfaifi, R. Balu, K. Chiang, N. R. Choudhury and N. K. Dutta, *ACS Catal.*, 2025, 9301–9345.
3 M. K. Debe, *Nature*, 2012, **486**, 43–51.
4 U. A. Paulus, A. Wokaun, G. G. Scherer, T. J. Schmidt, V. Stamenkovic, N. M. Markovic and P. N. Ross, *Electrochim. Acta*, 2002, **47**, 3787–3798.
5 H. Yang, Y. Liu, X. Liu, X. Wang, H. Tian, G. I. N. Waterhouse, P. E. Kruger, S. G. Telfer and S. Ma, *eScience*, 2022, **2**, 227–234.
6 Y. Deng, J. Luo, B. Chi, H. Tang, J. Li, X. Qiao, Y. Shen, Y. Yang, C. Jia, P. Rao, S. Liao and X. Tian, *Adv. Energy Mater.*, 2021, **11**, e2101222.
7 M. Lefèvre, E. Proietti, F. Jaouen and J. P. Dodelet, *Science*, 2009, **324**, 71–74.
8 Y. Zeng, C. Li, B. Li, J. Liang, M. J. Zachman, D. A. Cullen, R. P. Hermann, E. E. Alp, B. Lavina, S. Karakalos, M. Lucero, B. Zhang, M. Wang, Z. Feng, G. Wang, J. Xie, D. J. Myers, J.-P. Dodelet and G. Wu, *Nat. Catal.*, 2023, **6**, 1215–1227.
9 Q. Sun, X. Yue, L. Yu, F.-Z. Li, Y. Zheng, M.-T. Liu, J.-Z. Peng, X. Hu, H. M. Chen, L. Li and J. Gu, *J. Am. Chem. Soc.*, 2024, **146**, 35295–35304.
10 Z. Zhang, Z. Xing, X. Luo, C. Cheng and X. Liu, *Nat. Commun.*, 2025, **16**, 921.
11 G. Chen, Y. An, S. Liu, F. Sun, H. Qi, H. Wu, Y. He, P. Liu, R. Shi, J. Zhang, A. Kuc, U. Kaiser, T. Zhang, T. Heine, G. Wu and X. Feng, *Energy Environ. Sci.*, 2022, **15**, 2619–2628.
12 X. Fu, N. Li, B. Ren, G. Jiang, Y. Liu, F. M. Hassan, D. Su, J. Zhu, L. Yang, Z. Bai, Z. P. Cano, A. Yu and Z. Chen, *Adv. Energy Mater.*, 2019, **9**, e1803737.
13 X. Wan, X. Liu, Y. Li, R. Yu, L. Zheng, W. Yan, H. Wang, M. Xu and J. Shui, *Nat. Catal.*, 2019, **2**, 259–268.
14 Y. Li, S. Yin, L. Chen, X. Cheng, C. Wang, Y. Jiang and S. Sun, *Energy Environ. Mater.*, 2023, **7**, e12611.
15 J. Li, W. Xia, J. Tang, Y. Gao, C. Jiang, Y. Jia, T. Chen, Z. Hou, R. Qi, D. Jiang, T. Asahi, X. Xu, T. Wang, J. He and Y. Yamauchi, *J. Am. Chem. Soc.*, 2022, **144**, 9280–9291.
16 X. Wang, M. Yu and X. Feng, *eScience*, 2023, **3**, 100141.
17 X. Feng, Y. Bai, M. Liu, Y. Li, H. Yang, X. Wang and C. Wu, *Energy Environ. Sci.*, 2021, **14**, 2036–2089.
18 X. Guo, J. Shi, M. Li, J. Zhang, X. Zheng, Y. Liu, B. Xi, X. An, Z. Duan, Q. Fan, F. Gao and S. Xiong, *Angew. Chem., Int. Ed.*, 2023, **62**, e202314124.
19 X. Xu, H. Wu, Y. Yan, Y. Zheng, Y. Yan, S. Qiu, T. Liang, C. Deng, Y. Yao, J. Zou and M. Liu, *Adv. Energy Mater.*, 2025, **15**(20), e2405236.
20 L. L. Cui, Q. L. Zhang and X. Q. He, *J. Electroanal. Chem.*, 2020, **871**, 114316.
21 F. Liu, L. Shi, X. Lin, D. Yu, C. Zhang, R. Xu, D. Liu, J. Qiu and L. Dai, *Appl. Catal., B*, 2022, **302**, 120860.
22 H. Zhang, S. Hwang, M. Wang, Z. Feng, S. Karakalos, L. Luo, Z. Qiao, X. Xie, C. Wang, D. Su, Y. Shao and G. Wu, *J. Am. Chem. Soc.*, 2017, **139**, 14143–14149.
23 D. Deng, L. Yu, X. Chen, G. Wang, L. Jin, X. Pan, J. Deng, G. Sun and X. Bao, *Angew Chem., Int. Ed. Engl.*, 2013, **52**, 371–375.
24 Y. Hu, J. O. Jensen, W. Zhang, L. N. Cleemann, W. Xing, N. J. Bjerrum and Q. Li, *Angew Chem., Int. Ed. Engl.*, 2014, **53**, 3675–3679.
25 W. Zhang, P. Sherrell, A. I. Minett, J. M. Razal and J. Chen, *Energy Environ. Sci.*, 2010, **3**, 1286–1293.
26 L. D. Mansker, Y. Jin, D. B. Bukur and A. K. Datye, *Appl. Catal., A*, 1999, **186**, 277–296.
27 Y. Ren, Z. Ma, R. E. Morris, Z. Liu, F. Jiao, S. Dai and P. G. Bruce, *Nat. Commun.*, 2013, **4**, 2015.
28 F. Jaouen, J. Herranz, M. Lefèvre, J.-P. Dodelet, U. I. Kramm, I. Herrmann, P. Bogdanoff, J. Maruyama, T. Nagaoka, A. Garsuch, J. R. Dahn, T. Olson, S. Pylypenko, P. Atanassov and E. A. Ustinov, *ACS Appl. Mater. Interfaces*, 2009, **1**, 1623–1639.
29 S.-H. Yin, S.-L. Yang, G. Li, G. Li, B.-W. Zhang, C.-T. Wang, M.-S. Chen, H.-G. Liao, J. Yang, Y.-X. Jiang and S.-G. Sun, *Energy Environ. Sci.*, 2022, **15**, 3033–3040.
30 L. Jiao, J. Li, L. L. Richard, Q. Sun, T. Stracensky, E. Liu, M. T. Sougrati, Z. Zhao, F. Yang, S. Zhong, H. Xu, S. Mukerjee, Y. Huang, D. A. Cullen, J. H. Park, M. Ferrandon, D. J. Myers, F. Jaouen and Q. Jia, *Nat. Mater.*, 2021, **20**, 1385–1391.
31 W. J. Jiang, L. Gu, L. Li, Y. Zhang, X. Zhang, L. J. Zhang, J. Q. Wang, J. S. Hu, Z. Wei and L. J. Wan, *J. Am. Chem. Soc.*, 2016, **138**, 3570–3578.
32 B. Tang, Q. Ji, X. Zhang, R. Shi, J. Ma, Z. Zhuang, M. Sun, H. Wang, R. Liu, H. Liu, C. Wang, Z. Guo, L. Lu, P. Jiang, D. Wang and W. Yan, *Angew. Chem., Int. Ed.*, 2025, **64**, e202424135.
33 M. Xiao, L. Gao, Y. Wang, X. Wang, J. Zhu, Z. Jin, C. Liu, H. Chen, G. Li, J. Ge, Q. He, Z. Wu, Z. Chen and W. Xing, *J. Am. Chem. Soc.*, 2019, **141**, 19800–19806.
34 E. Luo, C. Wang, Y. Li, X. Wang, L. Gong, T. Zhao, Z. Jin, J. Ge, C. Liu and W. Xing, *Nano Res.*, 2020, **13**, 2420–2426.
35 N. R. Sahraie, U. I. Kramm, J. Steinberg, Y. Zhang, A. Thomas, T. Reier, J.-P. Paraknowitsch and P. Strasser, *Nat. Commun.*, 2015, **6**, e8618.
36 Q. Wang, Y. Yang, F. Sun, G. Chen, J. Wang, L. Peng, W. T. Chen, L. Shang, J. Zhao, D. Sun-Waterhouse, T. Zhang and G. I. N. Waterhouse, *Adv. Energy Mater.*, 2021, **11**, 2100219.
37 Y. R. Li, S. H. Yin, L. Chen, X. Y. Cheng, C. T. Wang, Y. X. Jiang and S. G. Sun, *Energy Environ. Mater.*, 2024, **7**, e12611.
38 Y. Zhou, G. Chen, Q. Wang, D. Wang, X. Tao, T. Zhang, X. Feng and K. Müllen, *Adv. Funct. Mater.*, 2021, **31**, 2102420.
39 S. Liu, C. Li, M. J. Zachman, Y. Zeng, H. Yu, B. Li, M. Wang, J. Braaten, J. Liu, H. M. Meyer, M. Lucero, A. J. Kropf, E. E. Alp, Q. Gong, Q. Shi, Z. Feng, H. Xu, G. Wang, D. J. Myers, J. Xie, D. A. Cullen, S. Litster and G. Wu, *Nat. Energy*, 2022, **7**, 652–663.
40 L. Peng, J. Yang, Y. Yang, F. Qian, Q. Wang, D. Sun-Waterhouse, L. Shang, T. Zhang and G. I. N. Waterhouse, *Adv. Mater.*, 2022, **34**, 2202544.
41 Z. Pei, H. Zhang, Y. Guo, D. Luan, X. Gu and X. W. Lou, *Adv. Mater.*, 2023, **36**, 2306047.